A Time-Marching Aeroelastic Method Applied to Propeller Flutter

Ross J. Higgins*, Antonio Jimenez-Garcia† and George N. Barakos‡
University of Glasgow, James Watt South Building, Glasgow, G12 8QQ, U.K.

Nicholas Bown§
Dowty Propellers, Anson Business Park, Cheltenham Road East, Gloucester, GL2 9QN, U.K.

A time-marching aeroelastic method developed for the study of propeller flutter is presented and validated. Propeller flutter can take many forms with stall, whirl and classical flutter being the primary responses. These types of flutter require accurate capture of the non-linear aerodynamics associated with propeller blades. Stall flutter in particular, due to the highly detached nature of the flow, needs detailed unsteady flow modelling. With the development of modern propeller designs potentially adjusting the flutter boundary and the development of faster computing power, CFD is required to ensure accurate capture of aerodynamics. This paper focuses on the validation of the aeroelastic method using the Commander propeller blade.

Nomenclature

Latin

c	=	Blade chord (m)
f_m^s	=	Modal force on solid s for the m-th mode (N/m.kg)
n_m^s	=	Number of modes for solid s (-)
p	=	Pressure (Pa)
$\mathbf{p}(p,t)$	=	Pressure vector at a point p, and at a time t (N/m^2)
$\mathbf{P}$	=	Position of node p (m)
R	=	Blade Radius (m)
$\mathbf{R_{i,j,k}}$	=	Vector of flux residual for the the cell i, j, k
$\mathbf{R}$	=	Rotation Matrix (-)
R/c	=	Blade Aspect Ratio (-)
Re	=	Reynolds number based on the rotor blade chord and tip-speed

*PhD Student, CFD Laboratory.
†Post-Doctoral Researcher, CFD Laboratory.
‡Professor, CFD Laboratory, corresponding author.
§Project Engineer, Dowty Propellers.

t = Time (s)

$\mathbf{t}$ = Translation Matrix (-)

$V_{i,j,k}$ = Volume of the cell i, j, k

$\mathbf{w}_{i,j,k}$ = Vector of conservative variables for the cell i, j, k

$w_i(x)$ = Interpolation weight (-)

Greek

α_m^s = Model amplitude of mode m of solid s (m/kg)

ζ_m = Damping coefficient (-)

ψ_m^s = Normalised m^{th} mode displacement of solid s (m/kg)

ψ^s = Normalised displacement of solid s (m/kg)

ω_m = Natural frequency of mode m

Acronyms

ADT = Alternating Digital Tree

ALE = Arbitrary Lagrangian Eulerian

BILU = Block Incomplete Lower-Upper

CFD = Computational Fluid Dynamics

CSD = Computational Structural Dynamics

CFL = Courant-Friedrichs-Lewy condition

HMB3 = Helicopter Multi-Block Solver 3

MLS = Moving Least Square

MUSCL = Monotone Upstream-centered Schemes for Conservations Laws

SAS = Scale-Adaptive Simulation

SVD = Singular Value Decomposition

URANS = Unsteady Reynolds-Averaged Navier-Stokes

Subscripts

i, j, k = Mesh cell indices

Introduction

Propeller flutter manifests in a variety of different ways. This includes classic, stall and whirl flutter. These types of flutter, particularly whirl and stall, require accurate capturing of the non-linear aerodynamics and structure. In stall flutter, the non-linear aerodynamics is a result of the detached flow-field which triggers the aeroelastic excitation. For whirl flutter, the non-linear aerodynamics is a result of the interaction between the blade root and spinner, along with the propeller wake interaction with the wing.

Successful capture of such aerodynamic interactions allows for increased accuracy in surface loads, and the increased accuracy in predicting the resultant flutter boundary. From this base, and with the development of faster computing power, a time-marching aeroelastic method has been developed which couples Computational Fluid Dynamics (CFD) and Computational Structural Dynamics (CSD). Flutter of any type is a result of a fluid-structure interaction and the method was derived based on this assumption.

Literature Review

The understanding of propeller stall flutter began with the analysis of the Spitfire blade by Sterne in 1945 [1]. Static experimental analysis was conducted to determine the flutter boundary of the propeller based upon the blade pitch angle and the propeller rotational velocity. Results of the experiment found that the blade would flutter at a much lower velocity within a specific pitch region. Further analysis found that this reduction in the flutter boundary corresponded to the presence of stall, and hence concluded that stall flutter was the cause of the observed reduction in propeller performance.

A similar static investigation was conducted by DOWTY Propellers in 1979 [2]. The aim was to determine the torsional stress levels, and hence the flutter characteristics, of the Commander propeller blade when spun at a fixed pitch over a range of rotational velocities. The torsional stress levels were measured via strain gauges placed along the propeller radius. During the first stage of the test, high levels of torsional stress were seen for a given pitch angle, with the test terminated due to excessive oscillations. Upon examination of the propeller apparatus, the propeller crosshead had failed and hence a redesign of the crosshead was required. Following this, overspeed and 30 minute power run tests were completed at lower blade pitch angles.

n 1985, Smith conducted a static experimental investigation into three prop-fan model propellers [3]. These models were designated the SR-2, SR-3 and SR-5, with the blades characterised via increasing levels of sweep from the unswept, SR-2, to the highly swept, SR-5. In a similar manner to the DOWTY test, for a fixed pitch angle, the propeller rotational velocity was increased to maximum before returning to its baseline value with the vibratory stress levels measured via strain gauges. A comparison was made to the work conducted in the NASA/Lewis wind tunnel facilities. In terms of amplitude and trend, close agreement was found between the two investigations. Smith found stall flutter to occur on both the SR-2 and SR-3 propeller blades, with stall flutter only occurring in the SR-5 blade at very high rotational

velocities.

Reddy and Kaza in 1989 conducted a numerical investigation into the SR-2 propeller [4]. They utilised the Gormont and Gangwani dynamic stall models to capture the non-linear aerodynamics associated with stall flutter. These dynamic stall models resulted in conservative boundaries when compared to the experimental data of Smith [3]. Both models, however, predicted the same trends as found in experiments.

In an earlier investigation conducted by Baker in 1955 [5] the effects of various parameters on the flutter boundary of an untwisted propeller blade were investigated. The investigation included the effects of the structural blade parameters, the blade geometry, and the freestream flow conditions. Baker concluded that the positioning of the section centre-of-gravity, introduction of sweep, increase in section thickness and Mach number all had a significant effect on the flutter boundary. To ensure satisfactory aerodynamic performance, thin aerofoil sections are required at high speed, so therefore any change in section thickness would decrease performance. Baker did note that the resultant flutter boundaries were not within the normal operating cruise conditions for typical propellers, and only during take-off, when the propeller pitch was high, there was a higher likelihood of stall flutter.

In 2007, Delamore-Sutcliffe conducted a numerical investigation of propeller stall flutter [6]. It involved the derivation of a non-linear aerodynamic model which focused on stalled cross sections. The aerodynamic model was validated via two-dimensional experimental results, and was coupled with the Brooks and Houbolt equations of motion for a rotating beam. Comparisons were made to the experimental results of Baker [5] with close correlation found between the results.

In 1956, Hubbard *et al.*followed on from the work conducted by Baker in which a static experiment investigation into four model propeller blades was conducted [7]. The primary aim was to determine the effect of Mach number and structural damping on the flutter boundary. During the experiment, strain gauges were used to measure the vibratory stress levels with runs conducted at a fixed pitch angle, only varying the rotational velocity.

Ognev in 2011 investigated different unsteady aerodynamic models and their influence on the determined flutter boundary [8]. It used Theodorsen's model, two cascade based models and a three-dimensional model. These models were coupled with linearised equations of motion and were compared to the experimental work of Hubbard *et al.*[7]. A fair agreement between the experimental and numerical results were found.

Summary of Findings

Based on the literature survey findings, it is evident that there is a potential for a propeller to suffer from stall flutter particularly during low speed flight regimes, e.g. take-off. Based upon experimental observations, it is often the 1 st blade torsional mode that is excited in stall flutter.

There has been many static experimental investigations conducted, all of which followed a similar test procedure in which the blade rotational velocity was increased at a fixed pitch angle. In terms of numerical studies, all have focused

on the inclusion of the non-linear aerodynamics via dynamic stall based models.

Based upon this, it is evident that an aeroelastic investigation into propeller stall flutter requires the following key components:

1: Accurate capture of the non-linear aerodynamics.

2: Accurate capture of the non-linear structural modes and frequencies, particularly the 1 st torsional mode.

3: Investigation to be conducted in low-speed flight regimes, with potential validation from a static experimental test case.

Computational Methodology: HMB3

For this investigation into propeller flutter, a time-marching aeroelastic method has been developed. This method involves the coupling between Computational Fluid Dynamic (CFD) and Computational Structural Dynamics (CSD).

Computation Fluid Dynamics

The Helicopter Multi-Block (HMB3) [9–12] code is used as the CFD solver for the present work. It solves the Navier-Stokes equations in integral form using the Arbitrary Lagrangian Eulerian (ALE) formulation, first proposed by Hirt [13], for time-dependent domains, which may include moving boundaries. The unsteady Reynolds-averaged Navier-Stokes equation are discretised using a cell-centred finite volume approach on a multi-block grid. The spatial discretisation of these equations leads to a set of ordinary differential equations in time,

$$\frac{d}{dt}(\mathbf{w}_{i,j,k}V_{i,j,k}) = -\mathbf{R}_{i,j,k}(\mathbf{w}) \tag{1}$$

where i, j, k represent the cell index, $\mathbf{w}$ and $\mathbf{R}$ are the vector of conservative variables and flux residual respectively and $V_{i,j,k}$ is the volume of the cell i, j, k. The upwind scheme of Osher and Chakravarthy [14] is used to discretise the convective terms in space, whereas viscous terms are discretised using a second order central differencing spatial discretisation. The Monotone Upstream-centred Schemes for Conservation Laws (MUSCL) by Leer [15] is used to provide third order accuracy in space. The HMB3 solver uses the alternative form of the van Albada limiter [16] in regions where large gradients are encountered mainly due to shock waves, avoiding non-physical spurious oscillations. An implicit dual-time stepping method is employed to performed the temporal integration, where the solution is marching in pseudo-time iterations to achieve fast convergence, which is solved using first-order backward differences.

The linearised system of equations is solved using the Generalised Conjugate Gradient method with a Block Incomplete Lower-Upper (BILU) factorisation as a pre-conditioner [17]. Because implicit schemes require small CFL during early iterations, some explicit iteration using the forward Euler method or the four stage Runge-Kutta method (RK4) by Jameson [18] should be computed to smooth out the initial flow. Multi-block structured meshes are used

with HMB3, which allow an easy sharing of the calculation load for parallel job. ICEM-Hexa™ of ANSYS is used to generate the mesh. An overset grid method is available in HMB3 [19], to allow for relative motions between mesh components.

The chimera method is based on composite grids, consisting of independently generated, overlapping non-matching sub-domains. Each of these sub-domains are referred to as a Levels and are sorted hierarchically, with higher levels having priority. The exchange of information between sub-domains is achieved through interpolation and by following a hierarchy of mesh levels [19].

Various turbulence models are available in the HMB3 solver, which includes several one-equation, two-equation, and four-equation turbulence transition models. Furthermore, Large-Eddy Simulation (LES), Detached-Eddy Simulation (DES), Delay-Detached-Eddy Simulation (DDES), and Scale-Adaptive Simulation (SAS) options are also available. For this study, the *URANS* equations are coupled with two-equation $k - \omega$ turbulence model, and this is compared to the *SAS* formulation.

Computational Structural Dynamics

The aeroelastic framework of HMB3 is based on the modal method [20]. This method uses externally computed structural modes and a mesh deformation module based on the inverse distance weighting interpolation. The modal approach was selected in order to reduce computational cost as it expresses solid deformations as functions of the structure's eigenmodes.

A NASTRAN finite element model is created in order to obtain the structural mode shapes and frequencies. The finite element model uses non-linear PBEAM elements to model the structure's mass and inertia distribution along the span, with rigid bars (RBAR) elements used to connect the PBEAM node to each of the fluid mesh points at the given section. A non-linear static analysis (SOL 106) is computed to obtain the mode shapes and frequencies, along with a static deformation to rigid loads.

At the beginning of each computation, the structural modes are interpolated from the CSD to the CFD grid. The interpolation is performed with the Moving Least Square method (MLS). This method is accurate as loads integrations and displacement computations are carried out on the CFD grid without interpolation. In addition to this, the relative deflection of a given solid in contact to another must be computed to ensure any deflection is transferred correctly.

Computation of Modal Loads and Amplitudes

The CFD computation is performed on the deformed mesh to obtain the solution at $t + \Delta t$. The pressure is then summed over the undeformed mesh points to compute the modal loads $f_m^s(t)$ on the solid (s) for the m-th mode at time t:

$$f_m^s(t) = \sum_{p=1}^{n_s} \mathbf{p}(p,t).\phi_m^s(p) \tag{2}$$

with n_s the number of CFD points on the solid s, $\mathbf{p}(p,t)$ the pressure at a point p in N/m^2, and $\phi_m^s(p)$ the mode displacement at the point p for the m-th mode of the solid s normalised by the generalised mass set to 1kg. The modal load unit is $N/m.kg$.

The shape of the solid s, $\phi^s(t)$, is described as a sum of eigenvectors ϕ_m^s :

$$\phi^s(t) = \phi_0^s + \sum_{m=1}^{n_m^s} \alpha_m^s(t)\phi_m^s \tag{3}$$

with n_m^s the number of modes on the solid s, and ϕ_0^s the undeformed shape. The problem is then reduced to solving for the coefficient α_m^s.

In the modal approach, the coefficient can be obtained by solving the following differential equation:

$$\frac{\partial^2 \alpha_m^s}{\partial t^2} + 2\zeta_m \omega_m \frac{\partial \alpha_m^s}{\partial t} + \omega_m^2 \alpha_m^s = f_m^s(t) \tag{4}$$

For stability purposes, the analysis is started with a strong damping coefficient of $\zeta_m = 0.2$ for each mode. This high structural damping is used to control the oscillations created during the initial steps of the simulation, due to the sudden change in the forces applied to a second order system. Once the solid reaches an acceptable level of deformation, the damping is then gradually brought to its final value of $\zeta_m = 0.01$.

Then, equation 4 is explicitly solved using the leap-frog method. To ensure stability of higher modal frequencies, each time-step is solved in N_i inner time-steps of size $\Delta t_i = \Delta t / N_i$. The modal force at the time $t_i = t + i\Delta t_i$ is :

$$f_m^s(t_i) = f_m^s(t) + \frac{i(f_m^s(t+\Delta t) - f_m^s(t))}{N_i} \tag{5}$$

The m-th amplitude α_m^s is then assessed for inner time-step $t_i + 1$:

$$[\alpha_m^s]_{t_i+1} = [\alpha_m^s]_{t_i} + \left[\frac{\partial \alpha_m^s}{\partial t_i}\right]_{t_i} \Delta t_i + \frac{1}{2}\left[\frac{\partial^2 \alpha_m^s}{\partial t_i^2}\right]_{t_i} \Delta t_i^2 \tag{6}$$

The time derivative of the amplitudes are then computed as:

$$\begin{aligned} \left[\frac{\partial^2 \alpha_m^s}{\partial t_i^2}\right]_{t_i+1} &= [f_m^s]_{t_i} - \omega_m^2 [\alpha_m^s]_{t_i} - 2\zeta\omega_m \left[\frac{\partial \alpha_m^s}{\partial t_i}\right]_{t_i} \\ \left[\frac{\partial \alpha_m^s}{\partial t_i}\right]_{t_i+1} &= \left[\frac{\partial \alpha_m^s}{\partial t_i}\right]_{t_i} + \frac{1}{2}\left(\left[\frac{\partial^2 \alpha_m^s}{\partial t_i^2}\right]_{t_i} + \left[\frac{\partial^2 \alpha_m^s}{\partial t_i^2}\right]_{t_i+1}\right)\Delta t_i \end{aligned} \tag{7}$$

A flow chart showing the different stages of the method is shown in Figure 1

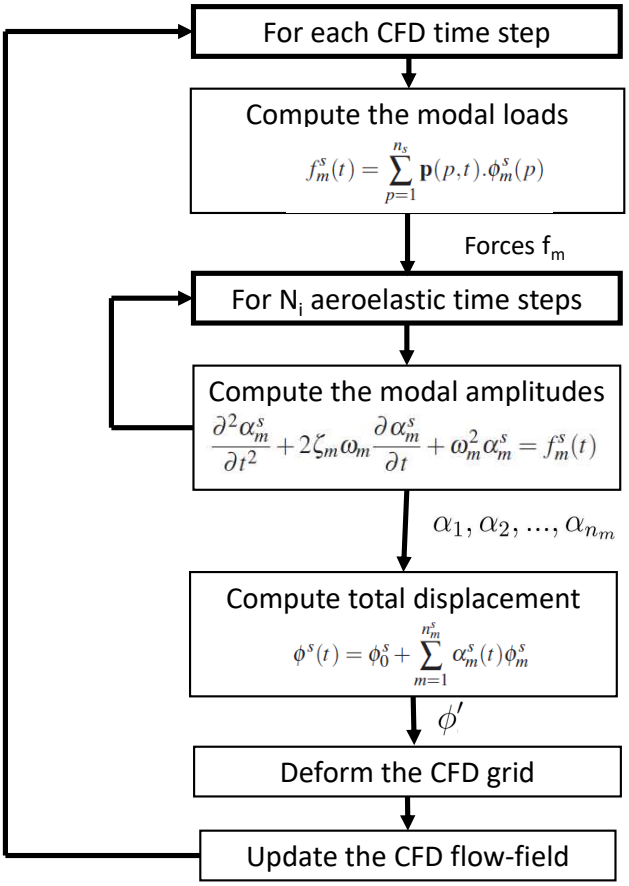

Fig. 1 Illustration of the computational structural dynamics strategy during each CFD time-step.

Surface Mesh Deformation

The displacement of the surface of each solid is computed using equation 3. The surface mesh is deformed then for each solid body, where the displacement due to the body is computed as:

$$\phi^f = \mathbf{RP} + \mathbf{t} \tag{8}$$

with **R** and **t**, respectively, the mean rotation matrix, and the translation vector of the shared points between the parent solid and its child, and **P** = [*x*, *y*, *z*] the position of the points of body f.

The translation vector is the mean displacement of the n_{sp} shared points between the parent body and its child:

$$\mathbf{t} = \frac{1}{n_{sp}} \sum_{p=1}^{n_{sp}} \phi^b(p) \tag{9}$$

with $\phi^b(p)$ the displacement of the point p imposed by the parent body. The centroids of the shared points are computed at the original position (A), and at the secondary position (B) imposed by the parent body:

$$\begin{aligned} \mathbf{C}_A &= \frac{1}{n_{sp}} \sum_{p=1}^{n_{sp}} \mathbf{P}(p) \\ \mathbf{C}_B &= \frac{1}{n_{sp}} \sum_{p=1}^{n_{sp}} (\mathbf{P}(p) + \phi^b(p)) \end{aligned} \tag{10}$$

The optimal solid rotation to go from position A to position B is computed with the Singular Value Decomposition technique (SVD). This method is fast and easy to implement [21]. The centers of both A and B are sent to the origin. Then, a covariance matrix $\mathbf{H}$ is computed:

$$\mathbf{H} = \sum_{p=1}^{n_{sp}} (\mathbf{P}(p) - \mathbf{C}_A)(\mathbf{P}(p) + \phi^b(p) - \mathbf{C}_B)^T \tag{11}$$

The singular value decomposition of the matrix is computed as:

$$[\mathbf{U}, \mathbf{S}, \mathbf{V}] = SVD(\mathbf{H}) \tag{12}$$

The rotation matrix is then given by:

$$\mathbf{R} = \mathbf{V}\mathbf{U}^T \tag{13}$$

Finally, the computed displacement with equation 8 and the displacement due to the structural modes are applied to the body.

Deformation of the Volume Mesh

To adapt the volume mesh to the surface of the deformed solid, a mesh deformation algorithm has been implemented in HMB3, based on Inverse Distance Weighting (IDW) [22]. IDW interpolates the values at given points with a weighted average of the values available at a set of known points. The weight assigned to the value at a known point is proportional to the inverse of the distance between the known and the given point. Biava *et al.*[23] used this method to optimise rotor blade shapes in HMB3, and obtained good quality mesh after mesh deformations.

Given N samples $\mathbf{u}_i = u(\mathbf{x}_i)$ for $i = 1, 2, ..., N$, the interpolated value of the function $\mathbf{u}$ at a point $\mathbf{x}$ using IDW is given by:

$$\mathbf{u}(\mathbf{x}) = \begin{cases} \dfrac{\sum_{i=1}^{N} w_i(\mathbf{x})\mathbf{u_i}}{\sum_{i=1}^{N} w_i(\mathbf{x})}, & \text{if } d(\mathbf{x}, \mathbf{x_i}) \neq \mathbf{0} \text{ for all } \mathbf{i} \\ \mathbf{u_i}, & \text{if } d(\mathbf{x}, \mathbf{x_i}) = \mathbf{0} \text{ for some } \mathbf{i} \end{cases} \tag{14}$$

where

$$w_i(\mathbf{x}) = \frac{\mathbf{1}}{\mathbf{d}(\mathbf{x}, \mathbf{x_i})^{\mathbf{p}}} \tag{15}$$

In the above equations, p is any positive real number (called the *power parameter*) and $d((\mathbf{x}), (\mathbf{y}))$ is the Euclidean distance between $(\mathbf{x})$ and $(\mathbf{y})$ (but any other metric operator could be considered as well).

The method in its original form becomes expensive as sample data sets get larger. An alternative formulation of the Shepard's method, which is better suited for large-scale problems, has been proposed by Renka [24] where the interpolated value is calculated using only the k nearest neighbours within an R-sphere (k and R are given, fixed, parameters) shown in green in Figure 2. The weights are slightly modified in this case:

$$w_i(\mathbf{x}) = \left(\frac{\max(\mathbf{0}, \mathbf{R} - \mathbf{d}(\mathbf{x}, \mathbf{x_i}))}{\mathbf{R}\mathbf{d}(\mathbf{x}, \mathbf{x_i})} \right)^{\mathbf{2}}, \quad \mathbf{i} = \mathbf{1}, \mathbf{2}, ..., \mathbf{k}. \tag{16}$$

If this interpolation formula is combined with a fast spatial search structure for finding the k nearest points, it yields an efficient interpolation method suitable for large-scale problems [22].

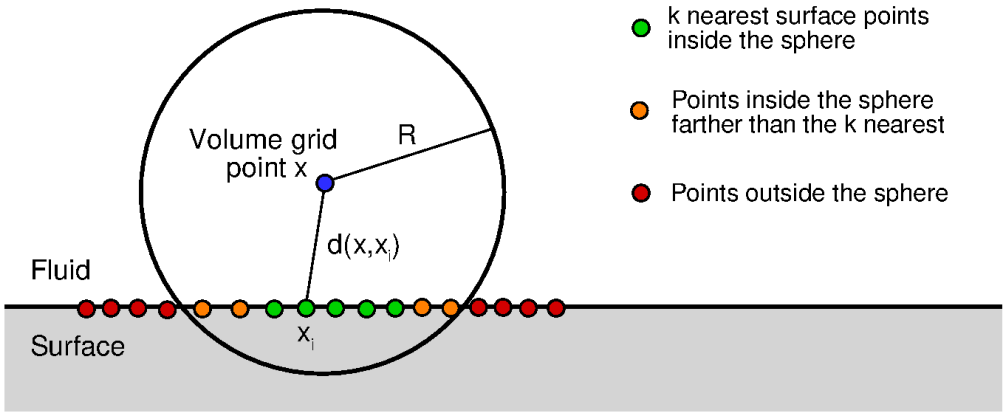

Fig. 2 Illustration of the point selection process in order to compute the IDW weights.

The modified IDW interpolation formula is used in HMB3 to implement mesh deformation in an efficient and robust way. The known displacements of points belonging to solid surfaces represent the sample data, while the displacements at all other points of the volume grid are computed using equation (14) with the weights of equation(16).

For fast spatial search of the sample points, an Alternating Digital Tree (ADT) data structure [25] is used. A blending function is also applied to the interpolated displacements, so that they smoothly tend to zero as the distance from the deforming surface approaches R.

Stall Flutter Cases

To conduct this investigation, the Commander propeller test case has been selected from which to study and validate the method. This test case was selected due to the availability of experimental data and its application it true engineering applications.

For all simulations, periodicity in space is assumed. This allows for the reduction of the computational domain to one propeller blade. The time-step for each calculation is selected to be $1 \circ$ in propeller revolution.

The structural model for the Commander blades are based upon the assumption of a solid material blade. The linear mass distribution is calculated as a function of the cross-section area, with the blade inertia based upon the variation in cross-section area.

Stall Flutter Investigation: Commander Propeller Blade

The Commander propeller blade was designed by GE-DOWTY in the 1970's and utilised aerofoil sections designed in collaboration with the Aerospace Research Association (ARA). Such aerofoil sections generated greater efficiencies and thus improved the take-off and climb performance of the aircraft.

The baseline propeller design consisted of three blades, with an aspect ratio of 10.9976 and chord of 0.129 m.

Computational Setup

Based upon the supplied geometry a computation domain of 120° was created with a radial distance from the origin of 5 R/c. The inflow was selected to be also 5 R/c with the outflow 8 R/c from the origin in the vertical direction. A solid cylindrical hub was created from the inflow to outflow.

An unmatched, chimera, grid was derived for this simulation. A chimera grid was selected to allow for the deflection of the blade during the aeroelastic computations. An O-grid was used for the foreground mesh and this was due to the blunt trailing edge and blade tip design. A conventional background grid was derived for the computational domain.

The baseline test conditions for this propeller were based upon the initial starting conditions of the static wind tunnel test conducted by DOWTY in the 1970's [2]. For this test case, sea-level conditions were assumed, with the reference velocity and length, for the Reynolds number, selected as the tip Mach number at 1400 (rpm) and tip chord length, respectively. Following the convergence of the rigid flow-field at 1400 (rpm), the aeroelastic module is introduced, with further details on its introduction presented in Section IV.A.2.

A single revolution is used to settle the structural response. Following this, the blade rotational velocity is

accelerated from 1400 to 1750 (rpm) over 5 revolutions. This acceleration mirrors the process conducted during the experiment. Table 1 details the flow computational parameters.

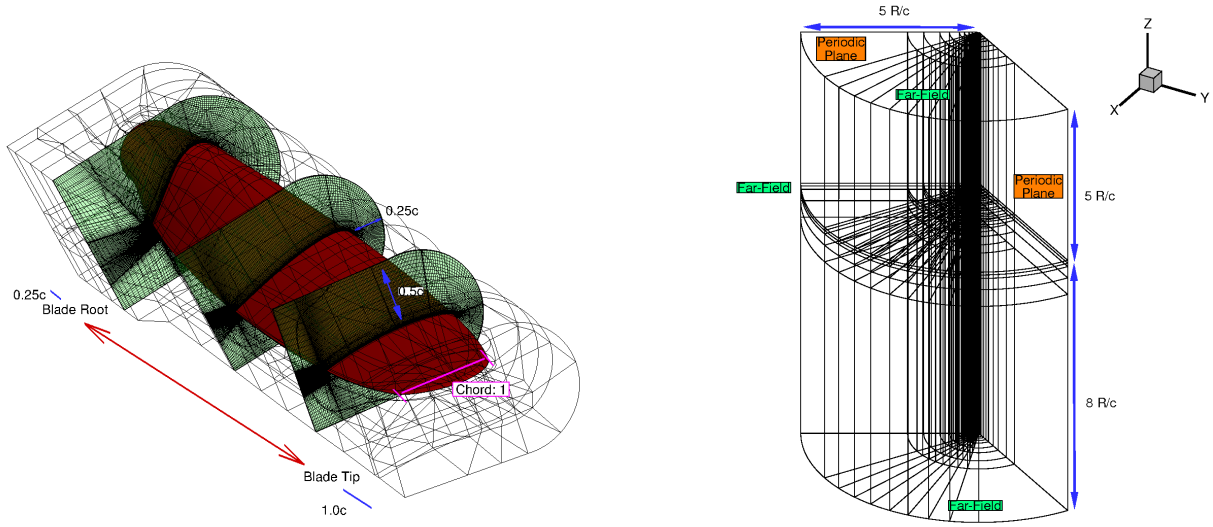

(a) Foreground Grid

(b) Background Grid

Fig. 3 Commander Propeller Computational Domain and Chimera Grid.

Reynolds Number (-)	1.65×10^6
Starting Propeller RPM (*RPM)*	1400
Final Propeller RPM (*RPM)*	1750
Blade Pitch Angle ($^\circ$)$_{0.70R}$	27° 40′
Altitude (*m)*	*Sea-level*
Inflow Velocity (*m/s)*	0.0 *(Static conditions)*
Tip Velocity (*m/s)*	197.36
Tip Chord Length (*m)*	0.122
Total Grid Size (*volume cells)*	12, 780, 064
Foreground	3, 532, 064
Background	9, 248, 000
Turbulence Model	*URANS* $k-\omega$ *& SAS*

Table 1 Summary of the Commander propeller blade test conditions.

Structural Modelling

The material properties of this model-scale blade are presented in Table 2. This blade was assumed to be of solid 1100 grade aluminum alloy. The cross-sectional area, linear mass and blade inertia's are presented in Figure 4.

Shown in Figure 5(a) is the blade mode shapes at the propeller starting velocity, with the frequencies presented in the Spoke diagram in Figure 5(b).

Young's Modulus (*Pa*)	6.9×10^{10}
Shear Modulus (*Pa*)	2.6×10^{10}
Mass Density (kg/m^3)	2710

Table 2 Commander Propeller Blade Material Properties.

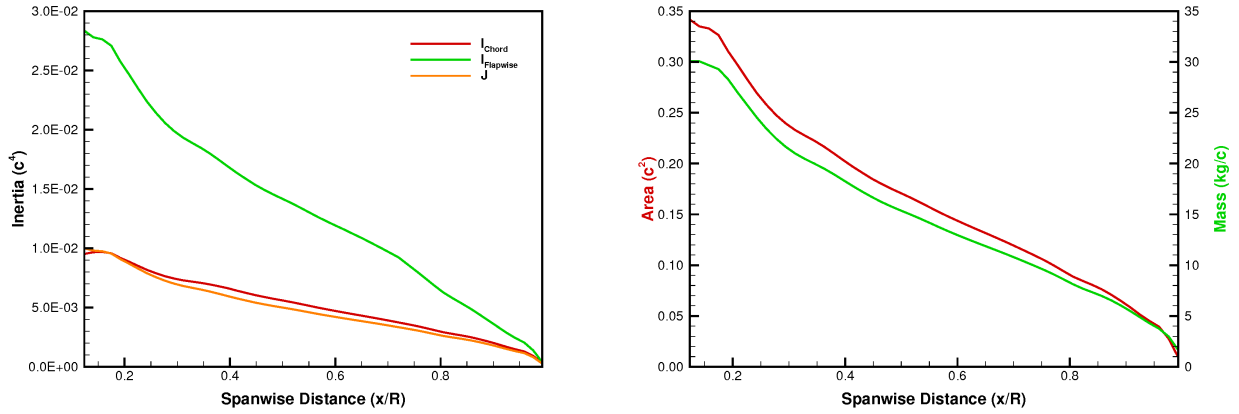

(a) Sectional Area and Mass

(b) Area moment of inertia

Fig. 4 Commander Propeller Blade Structural Properties

In terms of structural damping, a value is supplied to the modal method. For these calculations a transition was made from an initial high value of 0.10 to a final value of 0.001. This allows for the control of the initial aeroelastic response during the first aeroelastic revolution.

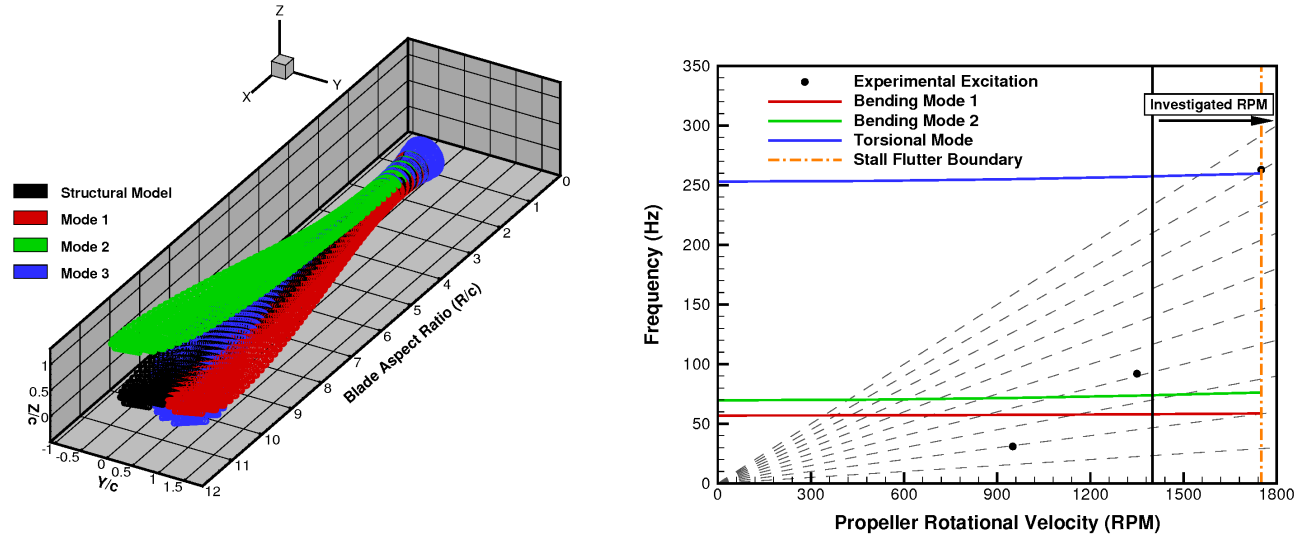

(a) Mode Shapes

(b) Spoke Diagram

Fig. 5 Commander propeller blade structural mode shapes and frequencies.

Simulation Results

A comparison is made between the *URANS* $k-\omega$ and *SAS* HMB3 simulations, and the experimental results of DOWTY. A qualitative comparison of the maximum qualitative torsional stress, along the blade radius, is presented in Table 3. The location of the maximum stress levels gives an indication of the amount of deflection presented at that station, and, in addition to this, the amount of stall. For the experimental results a value of 0.83 qualitative stress is seen at the 65% radial station. The stress levels then increase towards the tip, with a maximum value seen at 75%. After this maximum, the stress levels drop outboards of this section. A similar quadratic response is seen within the simulation results, however the location of maximum stress is slightly inboard, with respect to the experimental result, at 70%.

Radial Station	***Maximum Qualitative Torsional Stress***		
	Experiment	*URANS*	*SAS*
0.65	0.83	0.55	0.83
0.70	0.94	0.70	0.92
0.75	1.00	0.64	0.78
0.80	0.91	0.38	0.47
0.85	0.64	0.32	0.37
0.90	0.61	0.15	0.16

Table 3 Comparison of the maximum qualitative torsional stress, along the blade radius, between the experimental and simulation results.

In addition to the torsional stress levels, an analysis can be conducted on the structural response of the modal method. As the aeroelastic technique assumes the blade deflection is a combination of the supplied eigenmodes, modal amplitudes and forces are generated for each mode. Figure 6 presents the modal amplitudes for the three modes supplied. Looking at the first mode (chord-wise bending mode) an oscillating response of 2.54 Hz around a linearly increasing mean value is observed for the *URANS* simulation. A similar response is found for the *SAS* simulation, with a frequency of 2.46 Hz and linearly increasing mean, however the periodic amplitude increases for the *SAS* computation by 20% during the transition phase, and this increases by a factor of 3 during the final rotational velocity revolutions.

During the transition phase for the second mode, a decrease in periodic amplitude is found for the *SAS* simulation. This is a result of the current mode being a flap-wise bending mode. As previously described within Section III the modal amplitudes are calculated based upon the modal forces and these modal forces are a projection of the nodal point pressure onto the interpolated mode shape. Therefore, a decrease in modal amplitude indicates a decrease in modal force, and as a result a potential increase in detached flow due to the use of *SAS* . A decrease in modal force is observed in Figure 7. However, once the *SAS* simulation reaches the final rotational velocity, the periodic amplitude gradually increases to 66% of the transition value. No difference was found within the frequency response.

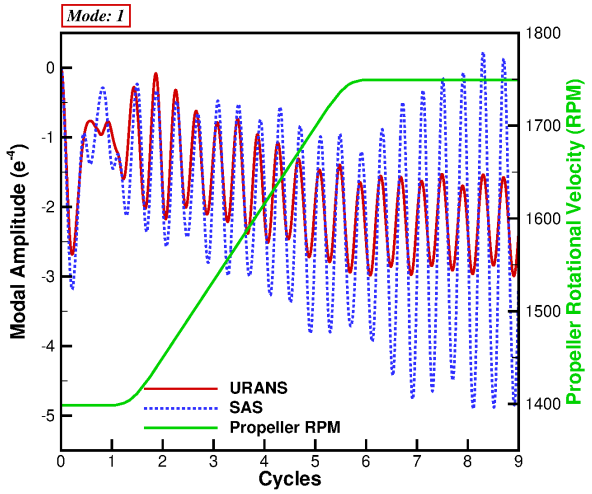

(a) Mode 1.

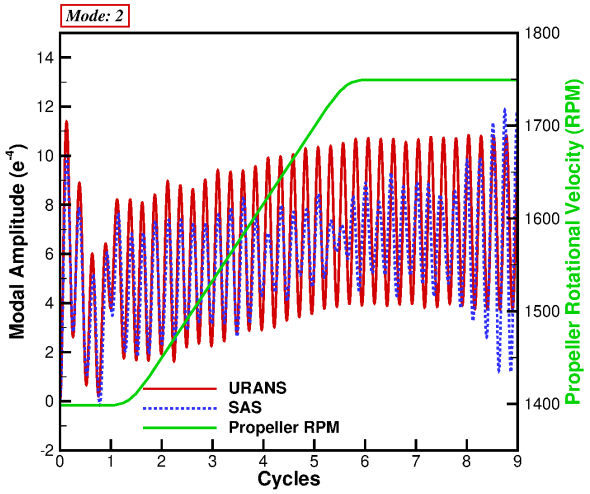

(b) Mode 2.

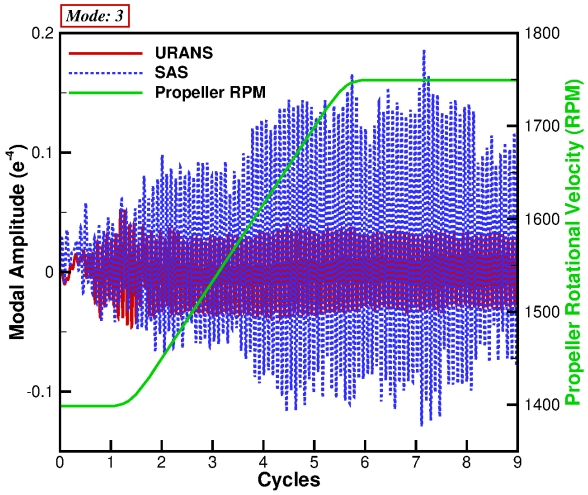

(c) Mode 3.

Fig. 6 Modal amplitude response for the Commander blade.

The most interesting, and most important, mode is the third mode as this is the first torsional mode. During the experiments of DOWTY, it was the third torsional mode which was triggered. For the *URANS* simulation, the modal amplitude oscillates around a constant mean value with a frequency of 11.3 Hz and periodic amplitude of 4×10^{-6}. As can be seen, this response is constant throughout the entire transition phase. For the *SAS* computation, the periodic amplitude grows during the transition phase, with a significant step change seen during the 4^{th} propeller revolution. During this step change the periodic amplitude increases by a factor of 2. The rotational velocity at this point is 1600 (rpm), and this correlates to the step change in torsional stress seen during the experiment. Once the acceleration is complete, the periodic amplitude continues to increase to 3 times the original transition value.

In terms of modal force, which is presented in Figure 7(c) for the third mode, the increase in torsional response is

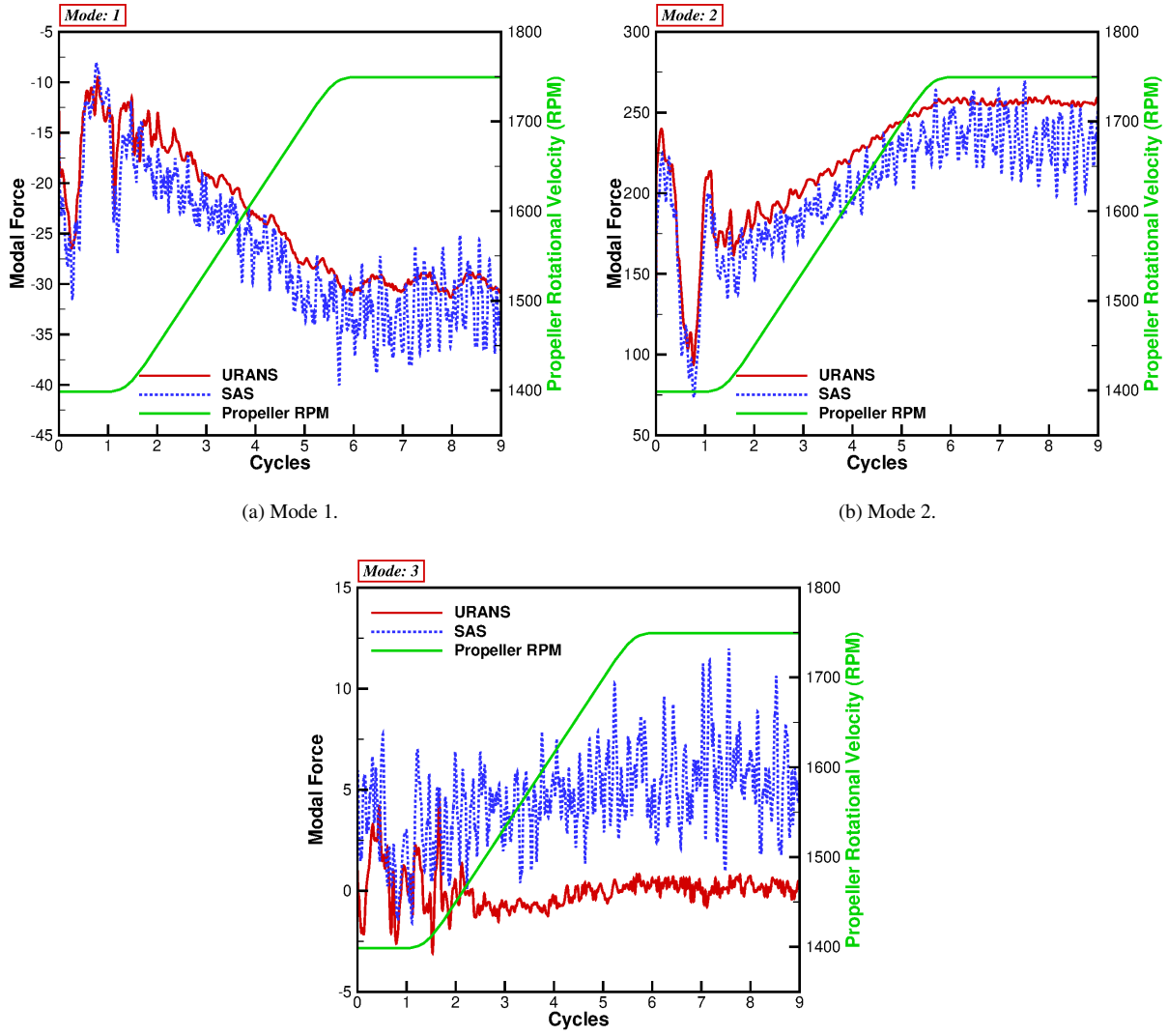

(a) Mode 1.

(b) Mode 2.

(c) Mode 3.

Fig. 7 Modal force response for the Commander blade.

seen due to the increase in modal force for the *SAS* simulation. This response is not observed for the *URANS* simulation as the torsional modal force is almost constant throughout the entire transition phase.

For the frequency response of the modal amplitude, a Fast-Fourier-Transform was conducted on each signal, and this is presented in Figure 8 for the *URANS* and *SAS* simulations. As can be seen for both computations, non-integer harmonics are present for all modes. This gives an indication of the presence of stall on the blade. The clear increase in amplitude for the *SAS* simulation can be seen, with additional fluctuations in the frequency response present due to the *SAS* formulation.

Presented in Figures **??** & **??** is the flow-visualisation, at the 70% radial station, of the non-dimensional vorticity magnitude with instantaneous streamlines for the *URANS* and *SAS* simulation, respectively, during the transition phase.

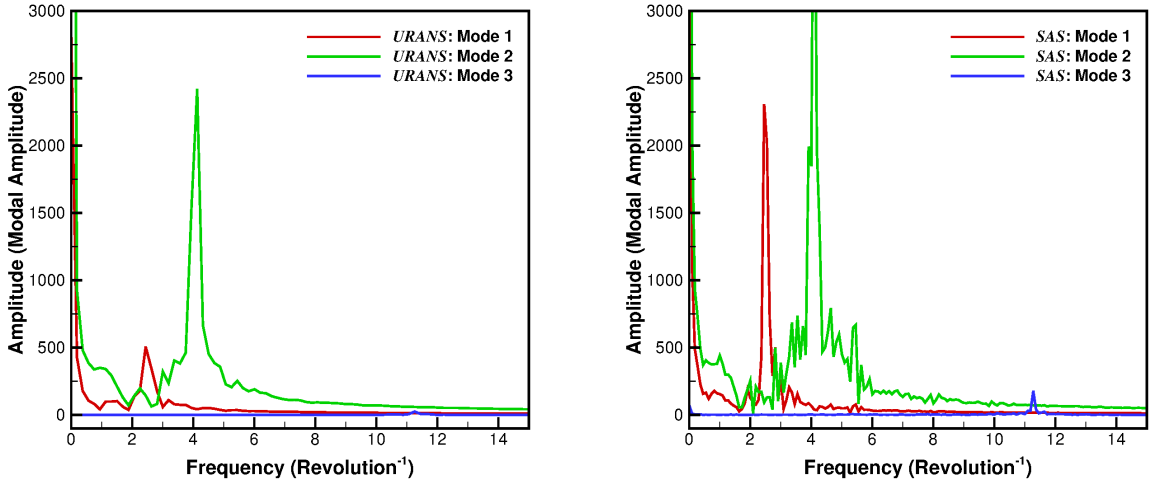

(a) *URANS* (b) *SAS*

Fig. 8 FFT of the modal amplitude response for the Commander blade.

As can be seen for the *URANS* simulation, an attached flow field is derived at this section. There is an increase in vorticity towards the leading and trailing edge of the aerofoil. The trailing edge vorticity is a result of the blunt aerofoil section, with the leading edge a result of the acceleration of the flow around the upper surface of the section. A similar profile is kept constant throughout the transition phase. The resultant flow for the *SAS* simulation is a great deal more active than the *URANS* result. The vorticity present at the leading edge of the *URANS* simulation is now detaching from the section. The flow attempts to reattach to the section, however due to the presence of the trailing edge vortex, is unable to. The trailing edge vorticity, seen in the *URANS* simulation, is now being projected upwards with the *SAS* model. As the flow is marched in time, this upwards projection causes a vortex to detach from the trailing edge. Once the vortex detaches it grows in size and dominates the flow-field. As the flow is accelerated, the leading edge vortex fluctuates in size, and, as it grows, begins to interact with the trailing edge vortex, before shedding entirely from the section.

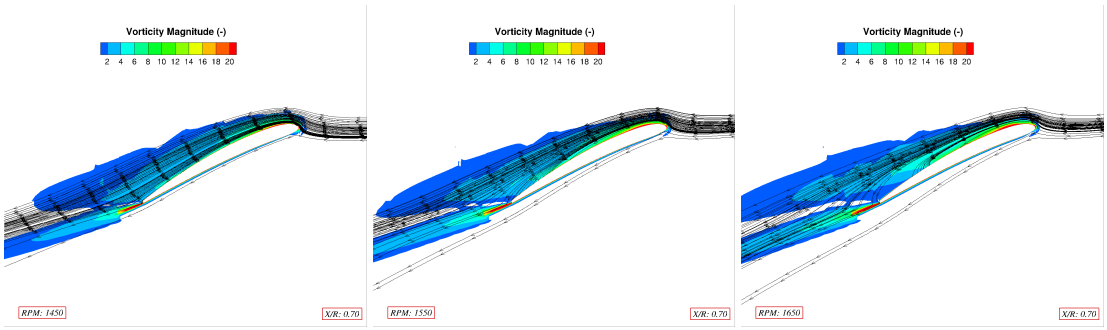

(a) *RPM*: 1450 (b) *RPM*: 1550 (c) *RPM*: 1650

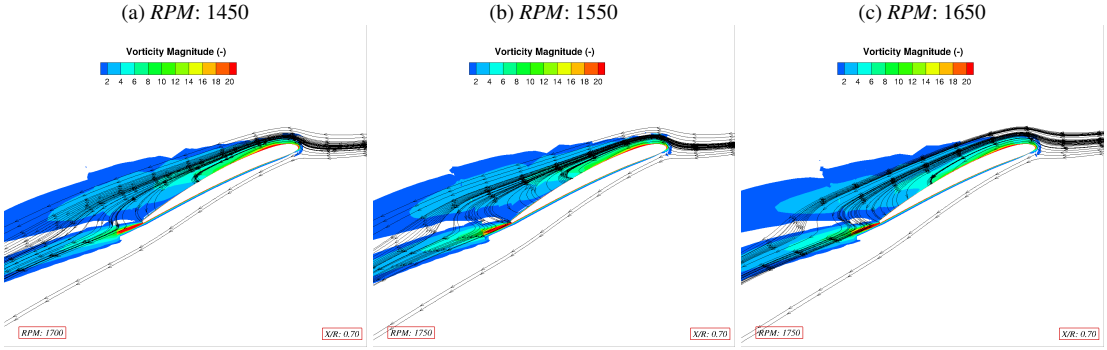

(d) *RPM*: 1700 (e) *RPM*: 1750 (f) *RPM*: 1750

Fig. 9 Flow visualisation at the 70% radial slice of the non-dimensional vorticity magnitude with instantaneous streamlines for the *URANS* simulation.

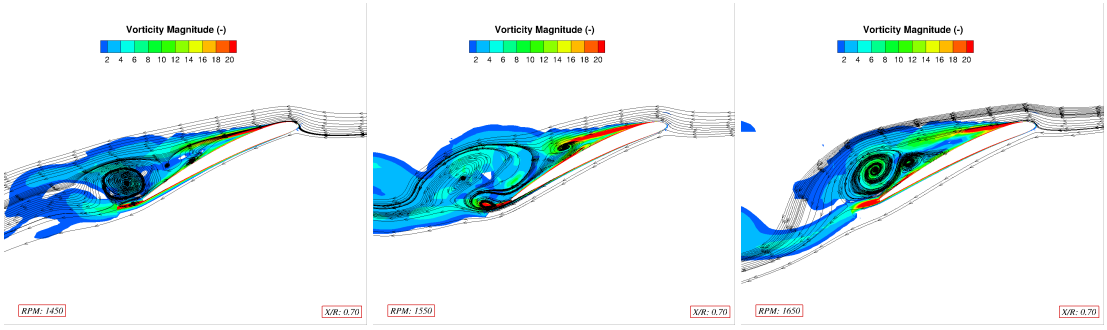

(a) *RPM*: 1450 (b) *RPM*: 1550 (c) *RPM*: 1650

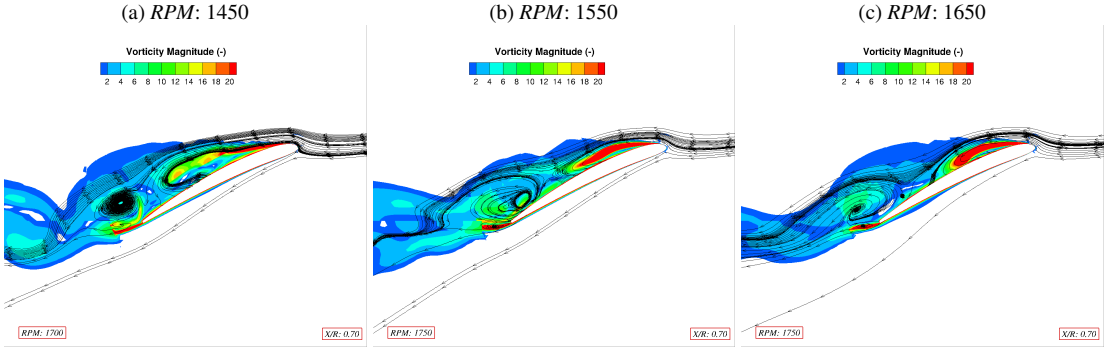

(d) *RPM*: 1700 (e) *RPM*: 1750 (f) *RPM*: 1750

Fig. 10 Flow visualisation at the 70% radial slice of the non-dimensional vorticity magnitude with instantaneous streamlines for the *SAS* simulation.

In a similar manner to the 70% section, the 90% radial station flow visualisation is presented in Figures 11 & 12. For the *URANS* simulation (Figure 11), the blade section is completely detached. Due to the formulation of the *URANS* equations, an entire detached flow bubble is produced. As can be seen during the transition, the bubble does not shed from the station. It is the shedding of the detached flow that causes the blade to flutter. Once the vortex is shed, the flow will attempt to reattach to the aerofoil section. This reattachment will cause a jump in the surface pressure, and hence blade loading. However, due to the nature of the flow, a detached vortex bubble will be generated, reducing the surface loading. This bubble will again shed, and the process will repeat. It is this phenomenon that is not captured via the standard *URANS* $k-\omega$ formulation.

This process is captured via the *SAS* simulation, shown in Figure 12. As was seen from the 70% station, the trailing edge vortex again interacts with the upper surface flow. As is seen from the *URANS* simulation, this station is completely stalled, and as a result, the trailing edge vortex has a greater influence. As can be seen in Figure 12(b), at 1550 (rpm), the trailing edge vortex has been projected onto the upper surface and partially detaching the stall bubble from the section. This causes the stall bubble to shed from the section (as is seen at 1650 (rpm)), with the trailing edge vortex collapsing. As the blade is accelerated, the rate of the shedding increases, along with the size of the generated stall bubble.

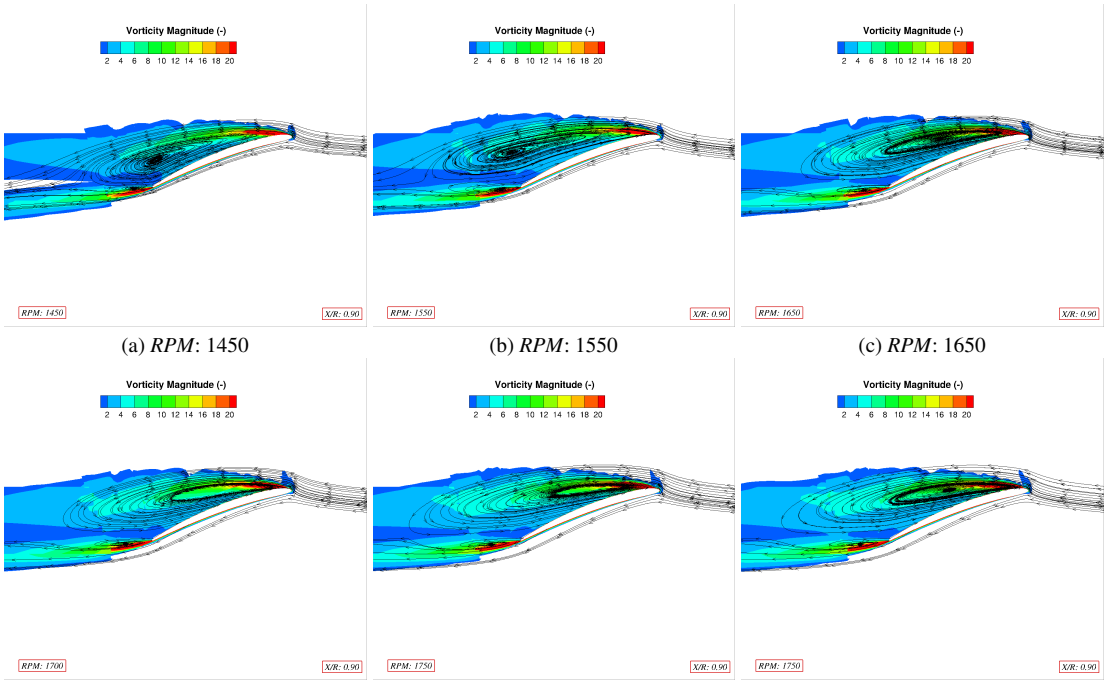

(a) *RPM*: 1450 (b) *RPM*: 1550 (c) *RPM*: 1650

(d) *RPM*: 1700 (e) *RPM*: 1750 (f) *RPM*: 1750

Fig. 11 Flow visualisation at the 90% radial slice of the non-dimensional vorticity magnitude with instantaneous streamlines for the *URANS* simulation.

The shedding shown at the 70% and 90% sections causes greater fluctuation in blade loading, which in turn causes an increase in the modal force variation. This variation in modal force, particularly for the torsional mode (mode 3), causes the increase seen in the periodic amplitude of the modal amplitude.

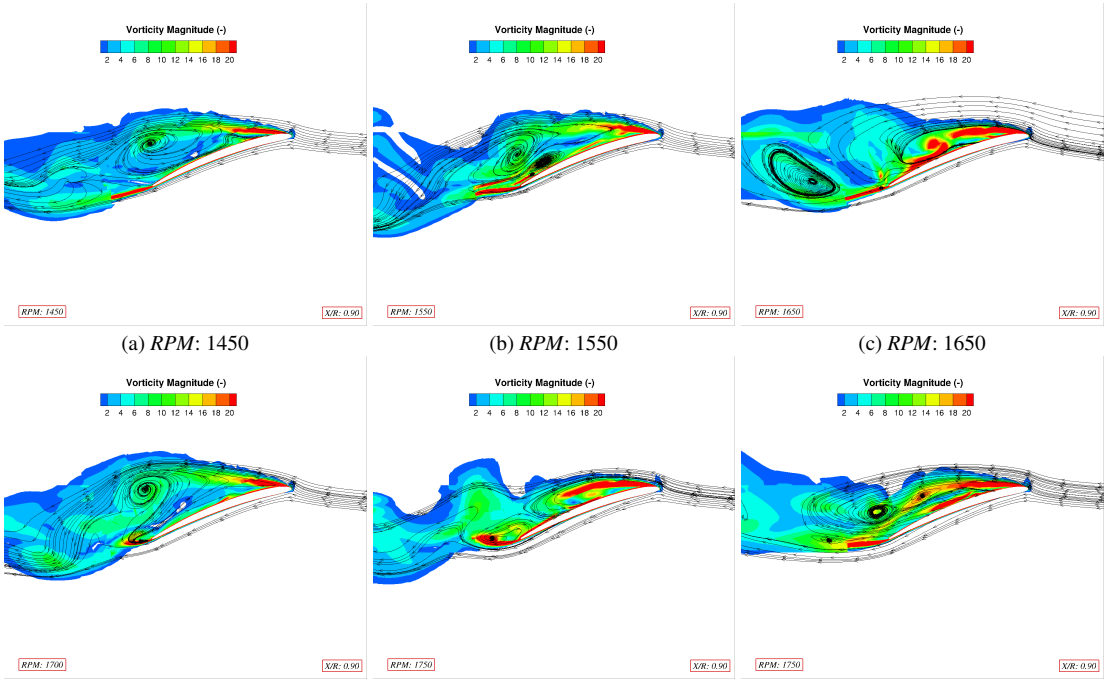

(a) *RPM*: 1450 (b) *RPM*: 1550 (c) *RPM*: 1650

(d) *RPM*: 1700 (e) *RPM*: 1750 (f) *RPM*: 1750

Fig. 12 Flow visualisation at the 90% radial slice of the non-dimensional vorticity magnitude with instantaneous streamlines for the *SAS* simulation.

In terms of the entire flow-field a visualisation of the vorticity magnitude iso-surfaces of value 1.0 is presented in Figures 13 & 14 for the *URANS* and *SAS* simulations, respectively. Looking at the *URANS* solution and focusing on the 1450 (rpm) visualisation, the detached flow bubble present towards the tip of the blade is clearly present, and projects until the inboard until the 70% station. Further towards the root, there is a detached flow bubble present towards the trailing edge of the blade. As the blade is accelerated, the inboard detached flow begins to interact with the tip bubble. In addition to this, the flow begins to detach at the root of the blade.

For the *SAS* simulation, again focusing on the 1450 (rpm) visualisation to start, from the 30% to 70% station the flow has detached at the trailing edge. Unlike the *URANS* iso-surfaces, there is a greater fluctuation in the *SAS* iso-surface flow structures. This is clearly seen at the tip detached flow section. As the blade is accelerated, the structure of the iso-surfaces continually alters and interacts with each other, due to the shedding of the vortical structures. In addition to the sectional detached flow interaction, due to the amount of stall present, there is a clear vortex interaction with the blade tip trailing vortex.

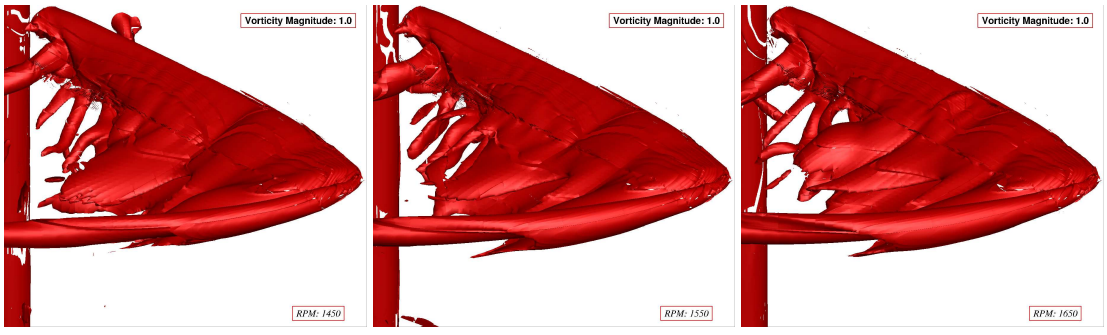

(a) *RPM*: 1450 (b) *RPM*: 1550 (c) *RPM*: 1650

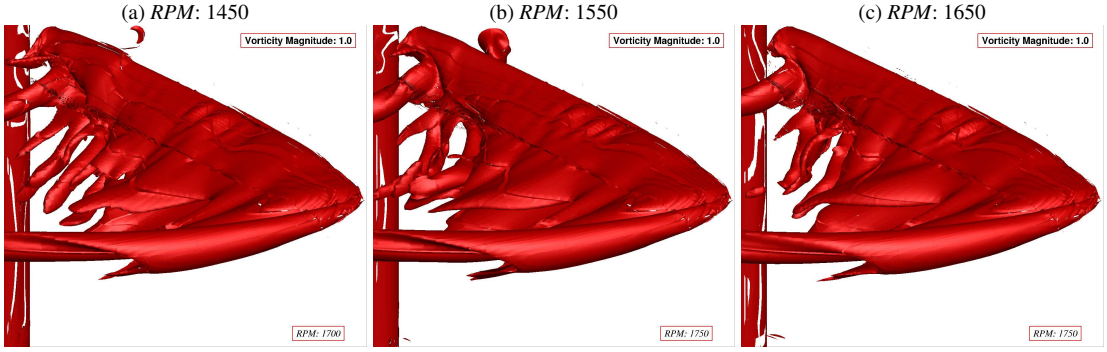

(d) *RPM*: 1700 (e) *RPM*: 1750 (f) *RPM*: 1750

Fig. 13 Flow visualisation of the vorticity magnitude iso-surface of value 1.0 **for the *URANS* simulation.**

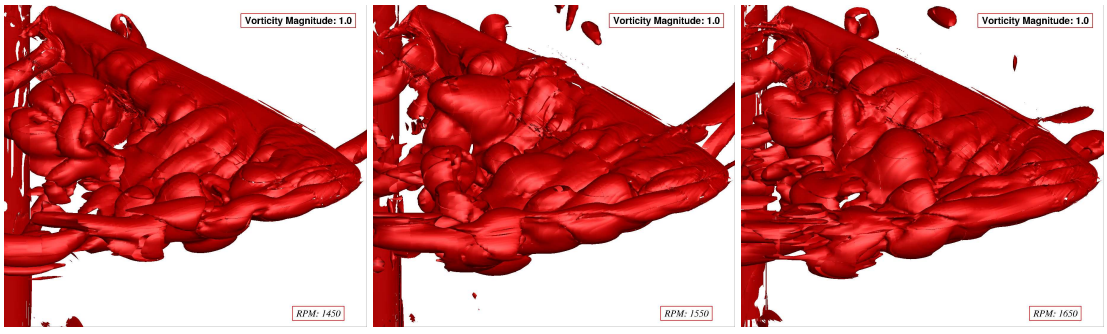

(a) *RPM*: 1450 (b) *RPM*: 1550 (c) *RPM*: 1650

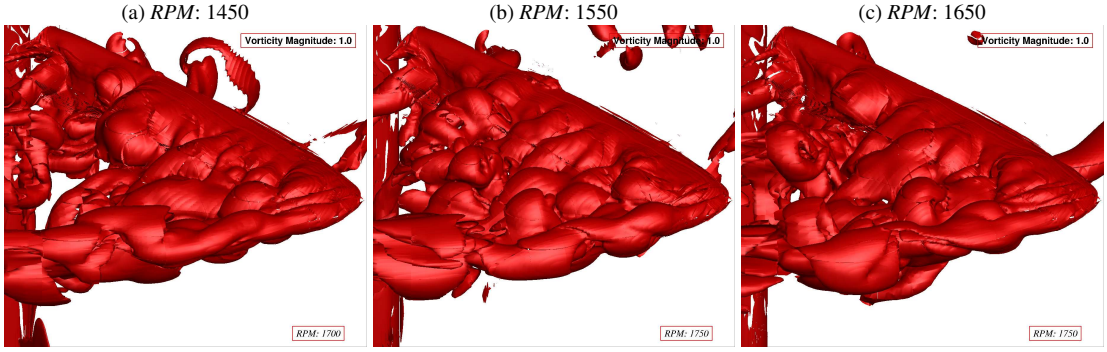

(d) *RPM*: 1700 (e) *RPM*: 1750 (f) *RPM*: 1750

Fig. 14 Flow visualisation of the vorticity magnitude iso-surface of value 1.0 **for the *SAS* simulation.**

Presented in Figures 15 & 16 are the surface pressure coefficients contours along the upper surface of the blade, during the acceleration, for the *URANS* and *SAS* simulations, respectively. As can be observed from the modal forces (Figure 7), there is an increase overall load due to the acceleration, however the profile of the spanwise load can be implied through the surface pressure contours.

For the *URANS* simulation in Figure 15, at the start of the simulation there appears to be a significant amount of stall acting along the blade. Flat pressure profiles are observed towards the tip and mid-span sections of the blade, with the 80% section showing a varying, hence attached flow, profile. As the blade is accelerated, lower pressure contours spread from the leading edge towards the trailing edge, with no significant variation in the overall pressure profile. A small pocket of higher pressure is created around the mid-chord section.

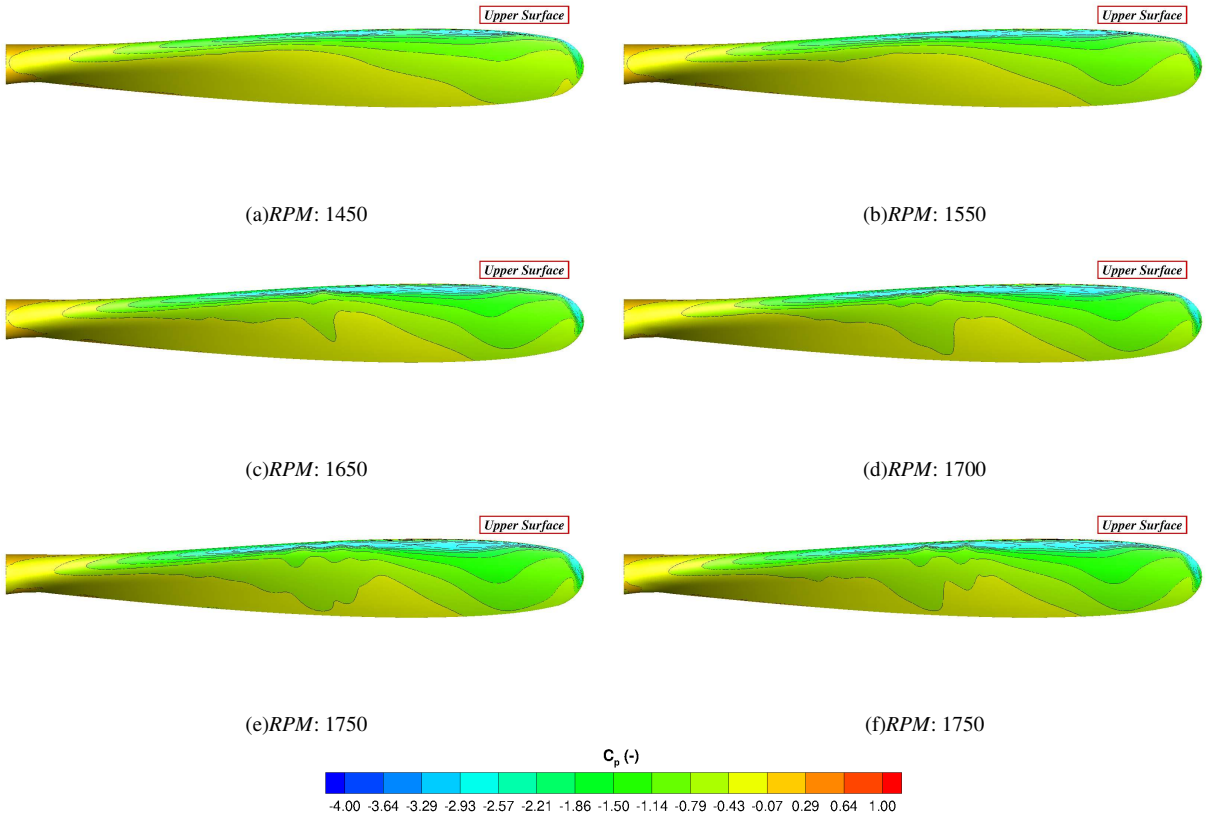

Fig. 15 Visualisation of the surface pressure coefficients for the *URANS* simulation.

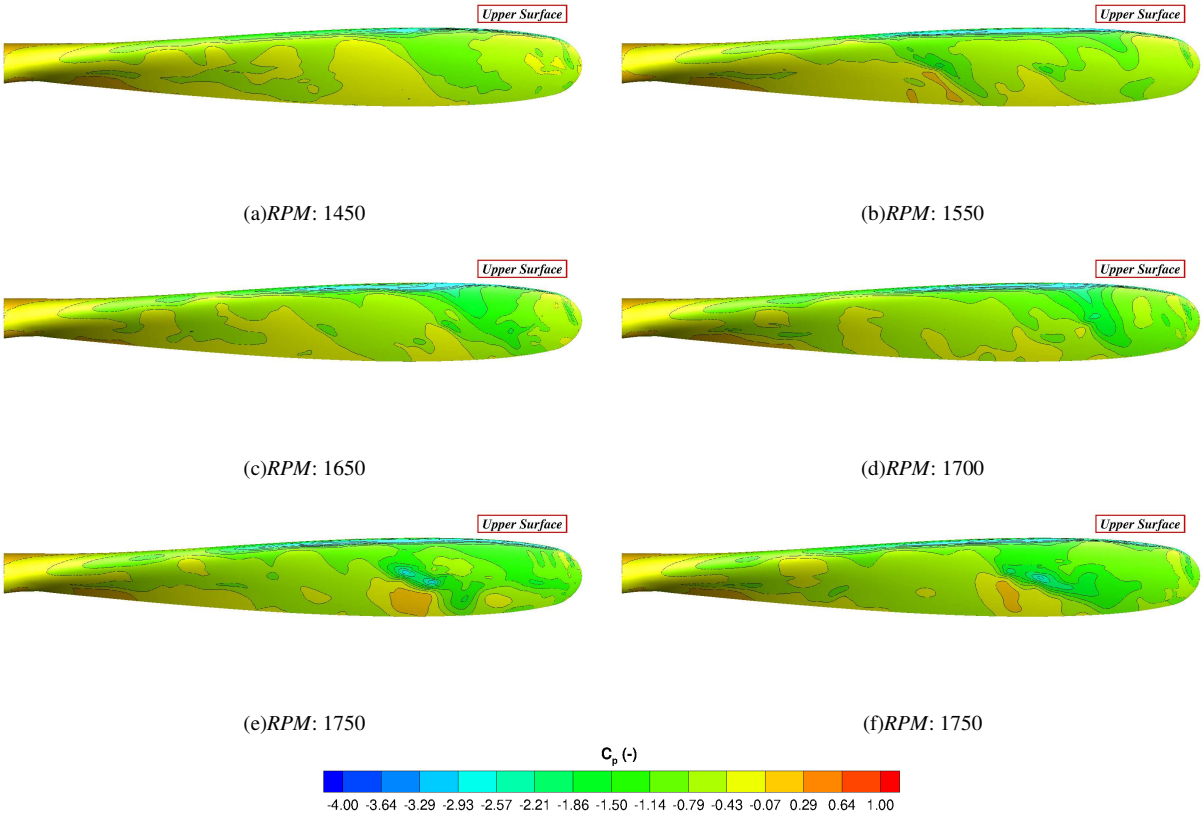

(a)*RPM*: 1450 (b)*RPM*: 1550

(c)*RPM*: 1650 (d)*RPM*: 1700

(e)*RPM*: 1750 (f)*RPM*: 1750

Fig. 16 Visualisation of the surface pressure coefficients for the *SAS* simulation.

Focusing on the *SAS* simulation, and as can be seen in Figure 16 a significant variation in the pressure profile is observed. Due to the increase in the amount of stall and shedding present along the blade. it is difficult to observe an overall profile during the transition. Similarities can be drawn between the *URANS* and *SAS* simulations; towards the tip of the blade an almost constant pressure contour is observed, with an increase in the amount of lower pressure seen during the acceleration. In addition to this, pockets of higher pressure are created during the acceleration. This is a result of the attempted reattachment of the flow to that section, as the vortex is shed from the blade.

In addition to the standard profile contours, a Fast-Fourier Transform was conducted on selected block faces of the propeller upper surface in terms of the surface pressure coefficient. This is shown in Figure 17 for the *URANS* and *SAS* simulations. As can be seen, a larger amount of frequency content is captured via the *SAS* simulation, with almost no significant peaks captured using *URANS* . In terms of the *SAS* , a significant spike at 5.5 Hz is captured.

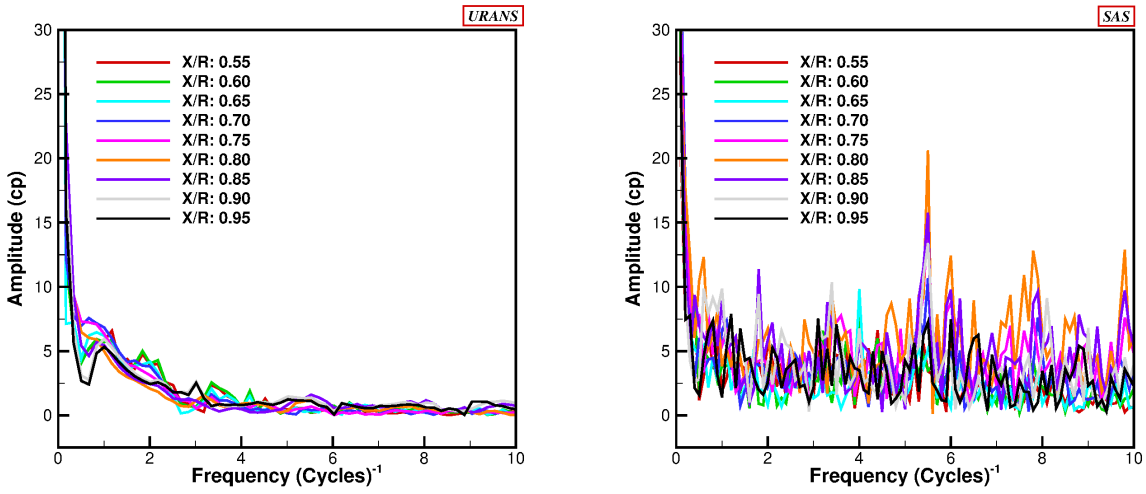

(a) *URANS* (b) *SAS*

Fig. 17 FFT of the surface pressure coefficient along the upper surface of the blade.

As previously described in Section IIIthe overall blade shape is a function of all three eigenmodes. The deflection of the given mode is multiplied by the modal amplitude and these deflections are summed over all modes to obtain a final shape. The shape of the Commander blade during the transition is presented in Figure 18 for the *URANS* and *SAS* simulations. The final shape for the elastic simulations, presented in Figure 18 have been scale by a factor of 500. This was to improve the visualisation of the defections in order to understand how the blade is reacting to the flow. The blade tip deflection for the *SAS* simulation at 1750 (rpm) is less than 0.1 (mm), hence the need for scaling.

As can be seen in Figure 18, the *URANS* and *SAS* simulations appear to have a similar response. As the blade is accelerated from 1400 to 1750 (rpm), the flapwise bending within the blade increases. This increase in flapwise bending can be inferred from the modal amplitudes shown in Figure 6. The second modal amplitude has the highest magnitude, followed by the first and then third, with the second mode being a flapwise bending mode. Due to the acceleration of the blade, and increase load applied within the vertical direction, the modal force for this flapwise mode increases. This in turn provides an increase in the modal amplitude.

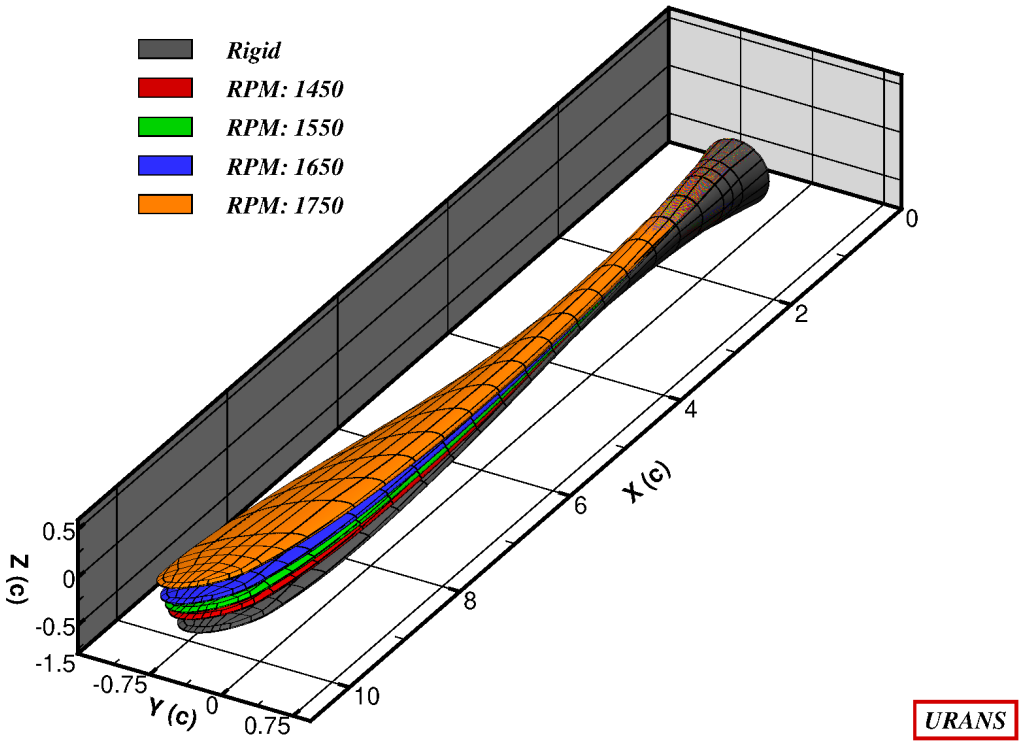

(a) *URANS*

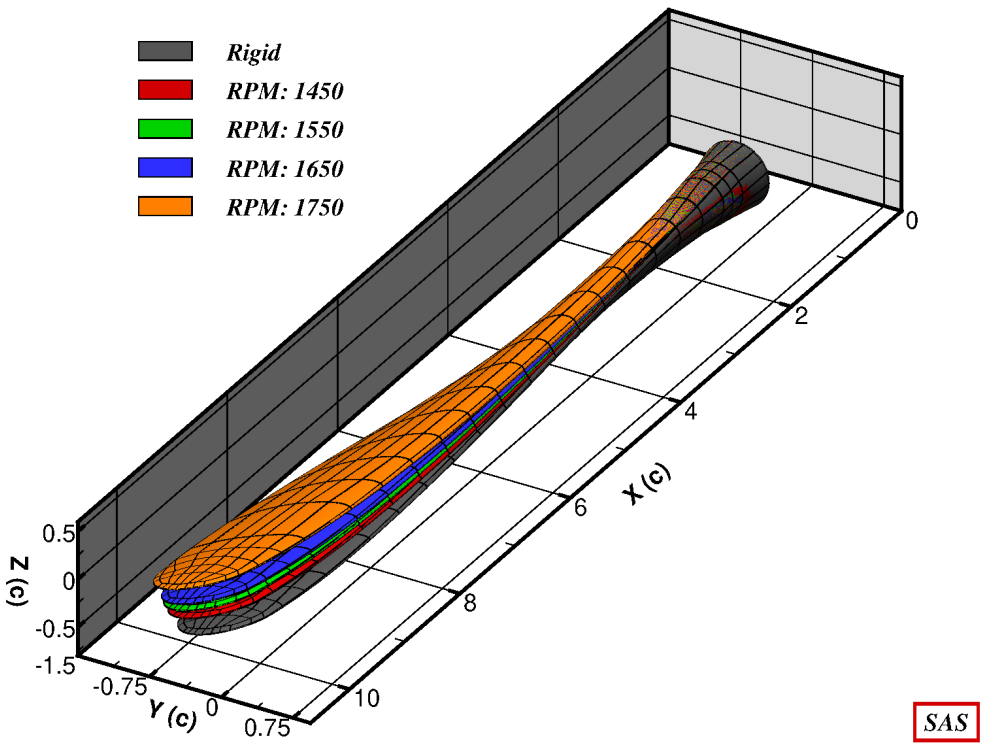

(b) *SAS*

Fig. 18 Comparison of the blade shape during the transition phase.

Conclusions and Future Work

Conclusions are now made based upon the results presented for the Commander propeller aeroelastic investigation:

- A successful time-marching aeroelastic method using CFD has been derived, with the quality of the computational mesh preserved throughout the calculation.
- For the Commander propeller blade, a qualitative agreement can be found between the simulation results and experimental.
- In order to improve the quantitative agreement, further analysis of the structural model is required.

In terms of future work, the following simulations are being investigated:

- Simulations are being conducted at fixed RPM in order to determine the effect of the transition on the modal amplitude response.
- An investigation into the structural model is being conducted, with new data being made available for the Commander blade.
- Simulations which couple directly NASTRAN and HMB3 are being investigated.

Acknowledgments

The support provided by DOWTY Propellers is gratefully acknowledged.

References

[1] Sterne, L., "Spinning Tests on Fluttering Propellers," *Aeronautical Research Council: Reports and Memoranda*, , No. 2022, 1945.

[2] Burton, P., "Straingauge Test Report on a Spin Test Carried out on a Type (c) R.305/3-82-F/6 Propeller on the Spinning Tower at the R.A.E. Farnborough, Hants." Tech. Rep. 093.1.592, DOWTY ROTOL LTD., 1979.

[3] Smith, A., "Analysis and Test Evaluation fo the Dynamic Stability of Three Advanced Turboprop Models at Zero Forward Speeds," Contractor Report 175025, National Aeronautics and Space Administration, 1985.

[4] Reddy, T., and Kaza, K., "Analysis of an Unswept Propfan Blade with a Semiempirical Dynamic Stall Model," Technical Memorandum, National Aeronautics and Space Administration, 1989.

[5] Baker, J., "The effects of various parameters, including Mach number, on propeller-blade flutter with emphasis on stall flutter," Tech. Rep. 3357, National Advisory Commitee for Aeronautics, 1955.

[6] Delamore-Sutcliffe, D., "Modelling of Unsteady Stall Aerodynamics and Prediction of Stall Flutter Boundaries for Wings and Propellers," Ph.D. thesis, University of Bristol, 2007.

[7] Hubbard, H., Burges, M., and Sylvester, M., "Flutter of thin propeller blades, including effects of Mach number, structural

damping, and vibratory-stress measurements near the flutter boundaries," Tech. Rep. 3707, National Advisory Commitee for Aeronautics, 1956.

[8] Ognev, V., and Rosen, A., "Influence of using various unsteady aerodynamic models on propeller flutter prediction," *Journal of Aircraft*, Vol. 48, No. 5, 2011.

[9] Lawson, S. J., Steijl, R., Woodgate, M., and Barakos, G. N., "High performance computing for challenging problems in computational fluid dynamics," *Progress in Aerospace Sciences 2012*, Vol. 52, No. 1, 2012, pp. 19–29. DOI: 10.1016/j.paerosci.2012.03.004.

[10] Steijl, R., and Barakos, G. N., "Sliding mesh algorithm for CFD analysis of helicopter rotor-fuselage aerodynamics," *International Journal for Numerical Methods in Fluids 2008*, Vol. 58, No. 5, 2008, pp. 527–549. DOI: 10.1002/d.1757.

[11] Barakos, G., Steijl, R., Badcock, K., and Brocklehurst, A., "Development of CFD Capability for Full Helicopter Engineering Analysis," *Proceedings of the Thirty-First European Rotorcraft Forum*, ERF, Florence, Italy, 2005, pp. 1–15.

[12] Steijl, R., Barakos, G. N., and Badcock, K., "A framework for CFD analysis of helicopter rotors in hover and forward flight," *International Journal for Numerical Methods in Fluids 2006*, Vol. 51, No. 8, 2006, pp. 819–847. DOI: 10.1002/d.1086.

[13] Hirt, C. W., Amsten, A. A., and Cook, J. L., "An Arbitrary Lagrangian-Eulerian Computing Method for All Flow Speeds," *Journal of Computational Physics*, Vol. 14, No. 3, 1974, pp. 227–253. DOI: 10.1016/0021-9991(74)90051-5.

[14] Osher, S., and Chakravarthy, S., "Upwind Schemes and Boundary Conditions with Applications to Euler Equations in General Geometries," *Journal of Computational Physics*, Vol. 50, No. 3, 1983, pp. 447–481. DOI: 10.1016/0021-9991(83)90106-7.

[15] van Leer, B., "Towards the Ultimate Conservative Difference Scheme. V. A Second-Order Sequel to Godunov's Method," *Journal of Computational Physics*, Vol. 32, No. 1, 1979, pp. 101–136. DOI: 10.1016/0021-9991(79)90145-1.

[16] van Albada, G. D., van Leer, B., and Roberts, W. W., "A Comparative Study of Computational Methods in Cosmic Gas Dynamics," *Astronomy and Astrophysics*, Vol. 108, No. 1, 1982, pp. 76–84.

[17] Axelsson, O., *Iterative Solution Methods*, Cambridge University Press, 1994.

[18] Jameson, A., Schmidt, W., and Turkel, E., "Numerical Solutions of Euler Equations by Finite Volume Methods Using Runge-Kutta Time-Stepping Schemes," *Proceedings of the Fourteenth Fluid and Plasma Dynamic Conference*, AIAA, Palo Alto, California, 1981, pp. 1–19.

[19] Jarkowski, M., Woodgate, M., Barakos, G., and Rokicki, J., "Towards Consistent Hybrid Overset Mesh Methods for Rotorcraft CFD," *International Journal for Numerical Methods in Fluids*, Vol. 74, No. 8, 2014, pp. 543–576. Doi:10.1002/fld.3861.

[20] Babu, S., Loupy, G., Dehaeze, F., Barakos, G., and Taylor, N., "Aeroelastic simulations of stores in weapon bays using Detached-Eddy Simulation," *Journal of Fluids and Structures*, Vol. 66, 2016, pp. 207–228. Doi:10.1016/j.jfluidstructs.2016.07.014.

[21] "Finding optimal rotation and translation between corresponding 3D points," http://nghiaho.com/?page_id=671, ???? Last accessed 9^{th} November 2017.

[22] Shepard, D., "A Two-dimensional Interpolation Function for Irregularly-spaced Data," *Proceedings of the 1968 23rd ACM National Conference*, New York, NY, USA, 1968.

[23] Biava, M., and Barakos, G., "Optimisation of Ducted Propellers for Hybrid Air Vehicles Using High-Fidelity CFD," *The Aeronautical Journal*, ????

[24] Renka, R., "Multivariate Interpolation of Large Sets of Scattered Data," *ACM Trans. Math. Softw.*, 1988, pp. 139 – 148. Doi:10.1145/45054.45055.

[25] Bonet, J., and Peraire, J., "An alternating digital tree (ADT) algorithm for 3D geometric searching and intersection problems," *International Journal for Numerical Methods in Engineering*, Vol. 31, No. 1, 1991, pp. 1–17. Doi:10.1002/nme.1620310102.